FULL PAPER

Electronic and Optical Properties of a Semiconducting Spinel (Fe_2CrO_4)

Scott A. Chambers, Timothy C. Droubay, Tiffany C. Kaspar, Iffat H. Nayyar, Martin E. McBriarty, Steve M. Heald, David J. Keavney, Mark E. Bowden, and Peter V. Sushko*

Epitaxial chromium ferrite (Fe_2CrO_4), prepared by state-of-the-art oxygen plasma assisted molecular beam epitaxy, is shown to exhibit unusual electronic transport properties driven by the crystallographic structure and composition of the material. Replacing 1/3 of the Fe cations with Cr converts the host ferrimagnet from a metal into a semiconductor by virtue of its fixed valence (3+); Cr substitutes for Fe at B sites in the spinel lattice. By contrast, replacing 2/3 of the Fe cations with Cr results in an insulator. Three candidate conductive paths, all involving electron hopping between Fe^{2+} and Fe^{3+}, are identified in Fe_2CrO_4. Moreover, Fe_2CrO_4 is shown to be photoconductive across the visible portion of the electromagnetic spectrum. As a result, this material is of potential interest for important photo-electrochemical processes such as water splitting.

1. Introduction

Transition metal oxides offer significant flexibility in tailoring functional properties by virtue of the high degree of solid solubility of different cations within the host lattice. For instance, the electronic properties of magnetite (Fe_3O_4), a ferrimagnetic half metal, can be substantially changed by substituting one third of the Fe cations with Mn, Ni, Co, Zn, or Mg. These substituents (which we will refer to as dopants) typically have the effect of converting the material into an insulator while allowing it to retain its ferrimagnetic character. The actual magnetic properties of any given ferrite depend critically on whether the dopant occupies the tetrahedral (A) or octahedral (B) sites, or a mix of the two.[1] New functionality would emerge if a dopant converts magnetite into a ferrimagnetic semiconductor. Such a ferrite would be of considerable interest for spintronics and photocatalysis, particularly if the bandgap remains small, enabling visible light harvesting. The detailed functional properties would depend on the local structure, which is dictated in large measure by the cation sublattice(s) the dopants occupy, the valence(s) they exhibit, and the relative energy scales of competing effects, including short-range disorder, that determine the overall electronic structure. Following our previous work using Cr dopants to engineer the bandgap of hematite, Fe_2O_3,[2,3] we have investigated Cr as a dopant in Fe_3O_4 by carrying out epitaxial film growth and characterization, along with first-principles modeling to explore new model materials.

In oxides, Cr exhibits stable valences of 3+ through 6+.[4] If Cr substitutes for Fe in Fe_3O_4, it can in principle occupy either tetrahedral or octahedral sites. Assuming substitutional Cr^{3+}, $Fe_{3-x}Cr_xO_4$ solid solutions should be stable without compensating defect formation for the concentration range $0 \le x \le 2$. Without defects, some fraction of the Cr ions would need to assume a 2+ valence for $x > 2$. The absence of naturally occurring oxides of Cr^{2+} suggests that intrinsically defect free $Fe_{3-x}Cr_xO_4$ cannot be made for $x > 2$. Accordingly, we consider the properties of $Fe_{3-x}Cr_xO_4$ within the composition space defined by $0 \le x \le 2$. We seek to know which of these solid solutions are at least partially conductive in the dark, ferrimagnetic at and above room temperature, and photoconductive in the visible portion of the electromagnetic spectrum. For $x \le 1$, charge hopping might be facile, depending on which cation sublattice (A or B) the Cr^{3+} cations occupy. Given that Cr^{3+} is found almost exclusively in octahedral coordination environments in other oxides, we expect that it will occupy B sites in the spinel lattice. As a result, Cr^{3+} should "pinch off" the B-site electron hopping path characteristic of magnetite to an extent that increases with x. First-principles modeling confirms these trends and predicts that a new conductive pathway, involving electron hopping between Fe cations at A and B sites, will become operative. If, however, Cr^{3+} were to occupy A sites, the B-site pathways would not be blocked and the conductivity should be approximately as it is in Fe_3O_4. At $x = 2$ ($FeCr_2O_4$), we expect that the material will be an insulator because electron hopping over any pathway would be quenched; electrons cannot hop between adjacent cation sites at all without temporally creating Cr^{2+}. Indeed, our calculations predict $FeCr_2O_4$ to be an insulator.

Dr. S. A. Chambers, Dr. T. C. Droubay,
Dr. T. C. Kaspar, Dr. I. H. Nayyar,
Dr. M. E. McBriarty, Dr. P. V. Sushko
Physical and Computational Sciences Directorate
Pacific Northwest National Laboratory
P.O. Box 999, Richland, WA 99354, USA
E-mail: sa.chambers@pnnl.gov
Dr. S. M. Heald, Dr. D. J. Keavney
Advanced Photon Source
Argonne National Laboratory
Argonne, IL 60439, USA
Dr. M. E. Bowden
Environmental Molecular Sciences Laboratory
Pacific Northwest National Laboratory
P.O. Box 999, Richland, WA 99354, USA

DOI: 10.1002/adfm.201605040

The electronic and optical properties of $Fe_{3-x}Cr_xO_4$ solid solutions have received relatively little attention, and all published studies to date are based on polycrystalline samples. Most previous work has focused on structural and magnetic properties[5–10] although charge hopping between Fe^{2+} and Fe^{3+} cations was inferred from Mossbauer spectroscopy.[11] Liu et al.[12] used crystal field theory to predict that Fe_2CrO_4 ($x = 1$) would be a half metallic ferrimagnet, but only if the Cr cations occupy A sites. Boudjemaa et al.[13] examined the photoelectrochemical properties of $FeCr_2O_4$ ($x = 2$) and claimed that the material is a p-type semiconductor because of the presence of cation vacancies. The electronic properties of $Fe_{3-x}Cr_xO_4$ are determined by the relative energies of the Fe and Cr t_{2g} and e_g band edges and the corresponding charge and spin distributions. To de-convolute the effect of substitutional Cr from other types of defects and fully understand the electronic, magnetic, and photoconductive properties of $Fe_{3-x}Cr_xO_4$, it is critical to carry out a controlled investigation of high-purity, single-crystalline films in combination with first-principles modeling. Here we focus on the cases of $x = 0$, 1, and 2 because they correspond to distinctly different electronic properties. Crystalline films of Fe_3O_4, Fe_2CrO_4, and $FeCr_2O_4$ supported on MgO(001) were prepared using oxygen assisted molecular beam epitaxy. Based on bulk crystallographic data, the in-plane lattice mismatches for Fe_2CrO_4 and $FeCr_2O_4$ on MgO(001) are −0.344% and −0.534%, respectively, which facilitates heteroepitaxy for both. We describe the materials properties of these films in the Supporting Information.

2. Results and Discussion

Figure 1 shows Fe 2p, Cr 2p, and O 1s core-level, as well as valence band (VB) X-ray photoemission spectra (XPS) for representative Fe_2CrO_4 and Fe_3O_4 films. We also include a Cr 2p reference spectrum for epitaxial α-Cr_2O_3 deposited on α-Al_2O_3(0001) in panel (b). The Cr 2p spectrum for Fe_2CrO_4 is quite similar to that of α-Cr_2O_3 for which a single valence (formally Cr^{3+}) is present throughout the lattice. The multiplet

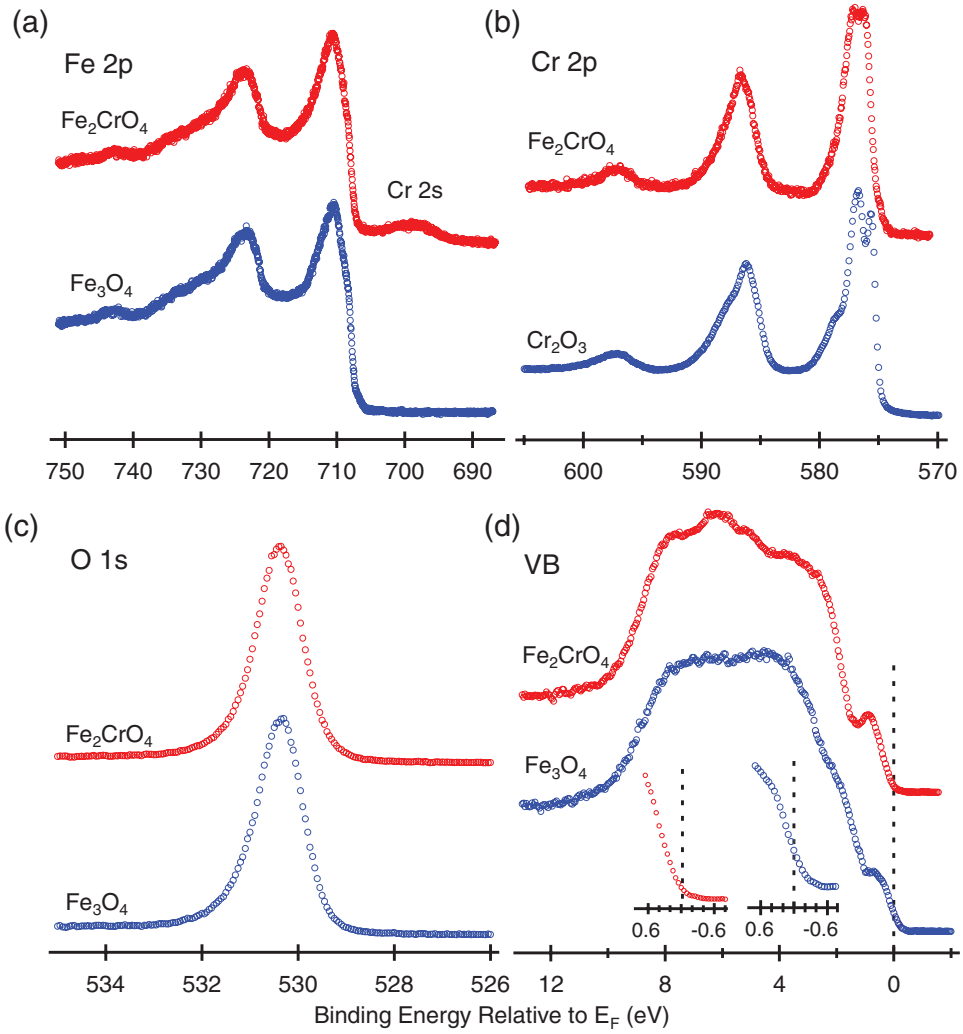

Figure 1. Core-level a) Fe 2p, b) Cr 2p, c) O 1s and d) valence band X-ray photoelectron spectra measured at normal emission for 100 nm epitaxial films of Fe_2CrO_4 and Fe_3O_4 on MgO(001), as well as for epitaxial α-Cr_2O_3 deposited on α-Al_2O_3(0001).

splitting and shake features in the Cr $2p_{3/2}$ manifold are slightly different between Fe_2CrO_4 and α-Cr_2O_3, but there is no evidence for any Cr formal charge other than 3+.[4,14,15] The Fe 2p spectra are very similar for Fe_3O_4 and Fe_2CrO_4. This result is rather surprising because the Fe^{2+} to Fe^{3+} cation number ratio is 1:2 in Fe_3O_4 and 1:1 in Fe_2CrO_4. In Fe_3O_4, the Fe 2p spectrum is typically interpreted as a complex mix of chemically shifted peaks associated with Fe^{2+} and Fe^{3+}, core hole-valence electron angular momentum coupled multiplets, and final-state shake features.[16] The relative intensities of the Fe^{2+} and Fe^{3+} features depend on the distribution of these species within the near-surface region and the surface termination. We thus conclude that the Fe cation distributions are different in $Fe_2CrO_4(001)$ than those in $Fe_3O_4(001)$. Indeed, angle-resolved measurements reveal that the intensity of the low-binding energy shoulder on the Fe $2p_{3/2}$ manifold at ≈708.2 eV (assigned to Fe^{2+}) relative to that for the larger peak at ≈710.2 eV (assigned to Fe^{3+}) decreases with increasing surface sensitivity, indicating that unlike $Fe_3O_4(001)$,[17] the near-surface region of $Fe_2CrO_4(001)$ is poor in Fe^{2+}. This depletion in Fe^{2+} in the near-surface region of Fe_2CrO_4 is a consequence of the mixed-valence nature of Fe in both A and B sites, which requires an electronic redistribution to maintain charge neutrality at the film surface, as described in more detail in the Supporting Information.

The O 1s spectra (Figure 1c) are also virtually identical for Fe_2CrO_4 and Fe_3O_4, exhibiting an asymmetry to higher binding energy resulting from electron–hole pair shake up (the Doniach–Sunjic lineshape[18]) consistent with both materials being conductive. The VB spectra (Figure 1d) differ in significant ways, reflecting the specific contributions of the two cations to the band structure. However, both spectra exhibit a distinct feature between 0 and 1 eV typically assigned to the Fe 3d minority t_{2g} band in Fe_3O_4 based on spin-polarized photoemission.[19] Expanded views shown as insets in Figure 1d reveal that the leading edge of the Fe_3O_4 VB strongly overlaps the Fermi level, but just reaches E_F for Fe_2CrO_4. This result suggests that Fe_2CrO_4 should be more resistive than Fe_3O_4. Indeed, transport measurements reveal this to be the case; the room-temperature resistivity of Fe_2CrO_4 films is ≈400 times higher than that measured for Fe_3O_4 films of the same thickness.

To determine how Fe and Cr are distributed among the A and B sites and gain insight into their atom-specific magnetic properties, we turn to K-shell extended X-ray absorption fine structure (EXAFS). The corresponding spectra are shown in **Figure 2**a, along with model fits described in detail in the Supporting Information. Fitting the EXAFS data reveals that Cr cations reside entirely at octahedral (B) sites. This result is consistent with the outcomes of first-principles calculations which reveal that the Fe_2CrO_4 lattice is more stable by ≈1 eV per atom when Cr occupies B sites compared to A sites. Thus, Fe cations occupy both A and B sites; the best fit to the EXAFS data indicates occupation with roughly comparable proportions (≈70% in A sites and ≈30% in B sites), as shown in Figure 2a. Analysis of the nearest-neighbor Fe–O distances reveals that for Fe in the tetrahedral sites, the fitted Fe–O distance (1.94 Å) lies between that for tetrahedral sites in the inverse spinel magnetite (1.887 Å, exclusively Fe^{3+}) and that for the normal spinel $FeCr_2O_4$ (1.997 Å, exclusively Fe^{2+}). We thus conclude that the tetrahedral sites contain a mix of Fe^{2+} and Fe^{3+}, as depicted in the idealized structural model in Figure 2a. Likewise, the fitted nearest-neighbor Fe–O distances in octahedral sites for Fe_2CrO_4 (2.06 and 2.07 Å) are consistent with the octahedral Fe–O distance in magnetite (2.060 Å, equal mix of Fe^{2+} and Fe^{3+}). Thus, Fe_2CrO_4 is neither a normal nor an inverse spinel.

In order to probe magnetic properties, we employ L-edge X-ray magnetic circular dichroism (XMCD), as shown in Figure 2b,c. The corresponding XAS data, which also reveal a mix of Fe^{2+} and Fe^{3+}, are shown in the Supporting Information. The Fe XMCD shows similarities to that exhibited by Fe_3O_4, but also show important differences.[20,21] For instance, the positive-going feature at 704 eV is not seen in the magnetite spectrum. This and other more subtle differences result from the different distributions of Fe^{3+} and Fe^{2+} on the A and B sites in the two lattices, as discussed in more detail below. The XMCD spectra reveal that the total magnetization is distributed among Cr^{3+}, Fe^{3+}, and Fe^{2+} cations. Vibrating sample magnetometry (VSM) indicates that Fe_2CrO_4 is ferrimagnetic with a total moment of 2.2 μ_B per f.u. over the temperature range 50–300 K (see Figure S6 in the Supporting Information). In order to interpret the XMCD data, we carried out simulations using the CTM4XAS code.[22] Our simulations are based on the assumptions that formal charges can be used to estimate the spin moments (Cr^{3+}: $3d^3 \rightarrow 3\ \mu_B$, Fe^{3+}: $3d^5 \rightarrow 5\ \mu_B$, Fe^{2+}: $3d^4 \rightarrow 4\ \mu_B$), and that the orbital contributions to the total moment can be neglected. As seen in Figure 2b,c agreement with experiment is excellent for the Cr L edge if we model Cr as being 3+, and occupying B sites. Our Cr L edge results are also in good agreement with those obtained earlier for a powder sample.[9] We modeled the Fe L edge by populating the A and B sites with both Fe^{2+} and Fe^{3+}. The individual spectra for the resulting four Fe environments are shown in Figure 2b, along with the weighted sum, which simulates the measured spectrum. The weighting factors that give the best agreement with experiment (discussed in more detail in the Supporting Information) reflect the Fe^{2+}-poor nature of the $Fe_2CrO_4(001)$ film surface. They also indicate that the B-site moments align parallel to one another and antiparallel to the A-site moments, as in other Cr containing spinels.[23,24] The dichroic sign modulation within the Fe L_3 manifold is very well reproduced using this model. However, the intensities of the first minimum at ≈702.5 eV and the first maximum at ≈704.0 eV are overestimated. Additionally, a weak minimum is predicted in the L_2 manifold at ≈720 eV, but is not observed, although the rest of the L_2 manifold is well reproduced. Overall, there is good agreement between the experimental and simulated spectra. These results provide insight into the magnitude of the volume-averaged magnetization by linking it to the charge redistribution between Fe cations in the A and B sites.

In particular, based on the idealized structure shown in Figure 2a, the local magnetic moment should exhibit values ranging from 2 to 4 μ_B per f.u., depending on the charges at the different Fe sites. The lower bound corresponds to the $[Fe^{3+}{}_AFe_B{}^{2+}Cr^{3+}{}_B][O^{2-}]_4$ configuration, with spins on the A sites being anti-parallel to spins on B sites. Electron transfer from Fe_B to Fe_A results in the $[Fe^{2+}{}_AFe_B{}^{3+}Cr^{3+}{}_B][O^{2-}]_4$ configuration, which corresponds to the upper bound on the magnetic moment. Assuming that both configurations can be realized, the average composition can be described as $(Fe_A{}^{2+})_\gamma(Fe_A{}^{3+})_{1-\gamma}(Fe_B{}^{2+})_{1-\gamma}(Fe_B{}^{3+})_\gamma(Cr^{3+})_1(O^{2-})_4$ ($0 \le \gamma \le 1$) and the corresponding magnetic moment is $2(\gamma+1)$ μ_B per f.u. This

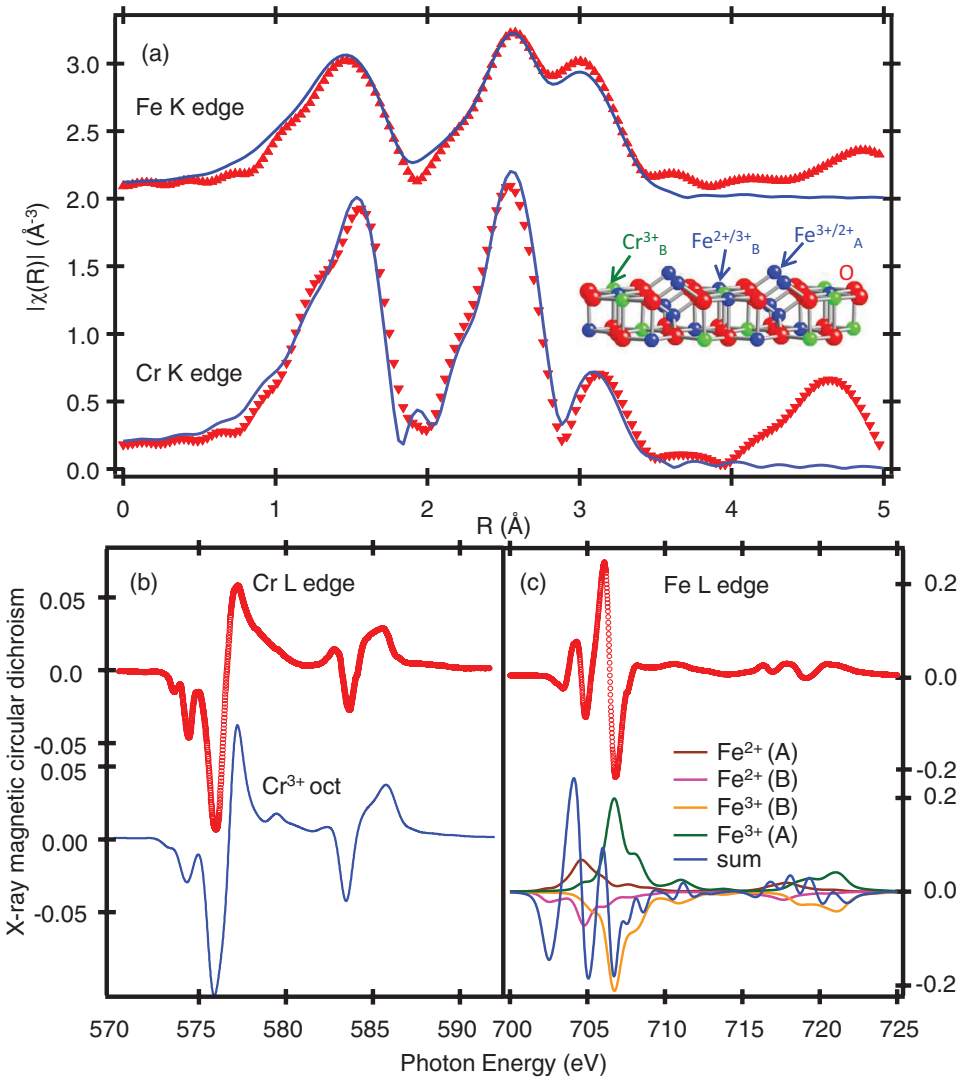

Figure 2. Measured (red) and simulated (blue) a) K-edge EXAFS and b,c) L-edge XMCD for representative epitaxial films of Fe_2CrO_4 on MgO(001). Also shown in (a) is an idealized spinel structure for Fe_2CrO_4, with mixed-valent Fe sites indicated. The XMCD is plotted as $2(I_R-I_L)/(I_R+I_L)$, where I_R (I_L) is the XANES measured with right (left) circularly polarized X-rays. The spectra were measured at $B = 0.5$ T and at room temperature. To accurately simulate the Fe L-edge XMCD spectrum, four configurations were included: Fe^{2+} at tetrahedral (A) sites, Fe^{2+} at octahedral (B) sites, Fe^{3+} at octahedral (B) sites and Fe^{3+} at tetrahedral (A) sites.

assumption is consistent with: (i) the results of our ab initio modeling which reveal that in the idealized structure, the total energies of the supercell for various values of γ are within 0.2 eV of one another and are thus nearly isoenergetic, and (ii) the experimental volume-average moment (2.2 μ_B per f.u.) is higher than that of the low-spin configuration.

XMCD reveals that Fe^{2+} is present in both A and B sites and, when combined with the total moment from VSM (2.2 μ_B per f.u.), allows us to estimate that ≈10% of A (B) sites are occupied with Fe^{2+} (Fe^{3+}) (i.e., $\gamma = 0.1$). There are thus three types of pathways for electron hopping as represented by the general formula $Fe_1^{2+}+Fe_2^{3+} \Rightarrow Fe_1^{3+}+Fe_2^{2+}$. One is B-to-B site hopping, similar to the dominant mechanism in Fe_3O_4. However, this pathway is likely to be highly resistive because only ≈10% of the B sites are available for hopping. Furthermore, the distance between neighboring Fe^{2+} and Fe^{3+} in B sites is effectively increased by the presence of Cr_B, which also decreases the probability of hopping along this path. A second pathway is A-to-A site hopping. The density of these paths is also low because only ≈10% of the A sites are populated by Fe^{2+}. The third pathway is hopping between A and B sites. However, the density of pathways that would facilitate B-to-A hops followed by A-to-B hops is also low because the fraction of Fe_A^{2+} and Fe_B^{3+} is only ≈0.1. Thus, all electron hopping pathways in Fe_2CrO4 are likely to be more resistive than the nearest-neighbor B-site hopping in Fe_3O_4, and experiment bears this out. A ρ (T) versus T curve for a representative film is shown in **Figure 3**a, with an Arrhenius plot of ln(ρ) versus T^{-1} in the inset. We see that $\frac{d\rho}{dT} < 0$, indicating semiconducting behavior. The resistivity becomes immeasurably high on our apparatus below ≈250 K. The slope of the Arrhenius plot yields an activation energy of ≈0.06 eV for

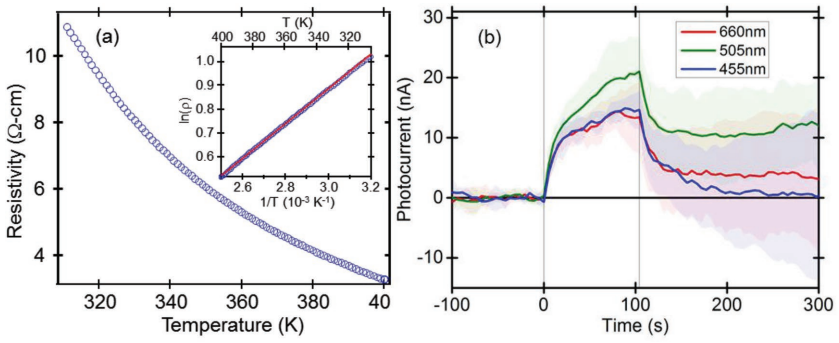

Figure 3. a) Resistivity versus temperature in the dark and b) D.C. photoconductivity for epitaxial Fe_2CrO_4 on MgO(001) under 0.10 ± 0.02 mW illumination at three wavelengths. Photoconductivity data are averaged between 5 and 6 individual measurements, with standard deviations shown as transparent envelopes.

electron hopping near room temperature. Substitution of Cr^{3+} for half the Fe cations within the B-site sublattice thus converts the material from a correlated half metal to a semiconductor.

To determine if additional carriers are readily generated by visible light absorption, we turn to D.C. photoconductivity measurements. Figure 3b shows the D.C. photocurrent response for illumination at three wavelengths: 660 nm (1.87 eV), 505 nm (2.46 eV), and 455 nm (2.72 eV), all of which are absorbed by Fe_2CrO_4, as seen in the Supporting Information. The dark D.C. current (linearly fitted over the 50 s preceding light on at $t = 0$ and subtracted off) was ≈80 μA for a 10 V bias across electrodes on the film surface, and illumination adds ≈10–20 nA of photocurrent. The material responds rather slowly, requiring of the order of 100 s for the photocurrent to saturate after the onset of illumination. Likewise, tens of seconds are required for the photocurrent to dissipate when illumination ceases. Because of the large, slowly varying background current, photocurrent rise and decay rates could not be accurately measured.

Incident (IPCE) and absorbed (APCE) photon-to-electron conversion efficiencies are calculated from the DC photoconductivity and presented in **Table 1**. APCE is calculated by dividing IPCE by the total light absorption in the film at each wavelength (see Figure S7, Supporting Information). The APCE values are nearly the same within error at the three wavelengths investigated, with a value of 0.04% after 10 s (the "fast" PC step), increasing to 0.06%–0.09% after 100 s. These energy conversion efficiencies are at least two orders of magnitude smaller than those measured by Klahr et al.[25] for hematite (α-Fe_2O_3) thin films under photoelectrochemical conditions. However, several factors preclude a direct quantitative comparison between these results. A photoelectrochemical cell such as that employed by Klahr et al. would be expected to operate at much smaller applied potentials and would experience efficiency losses due to charge transfer kinetics at the electrode–electrolyte interface. However, the perpendicular conduction path through a thin film would be orders of magnitude shorter than across the film (as in our circuit), dramatically improving efficiency. The consistent performance of Fe_2CrO_4 across the visible spectrum merits additional study of this material as an Earth-abundant photoanode for solar water splitting.

Table 1. IPCE and APCE for a 100 nm Fe_2CrO_4 epitaxial film calculated from DC photoconductivity at times t in Figure 3b. Values in parentheses indicate the error on the last digit.

	IPCE ($\times 10^{-4}$)		APCE ($\times 10^{-4}$)	
Wavelength [nm]	$t = 10$ s	$t = 100$ s	$t = 10$ s	$t = 100$ s
660	1.6(4)	3(1)	4(1)	6(3)
505	2.6(7)	5(2)	4(1)	9(3)
455	2.4(7)	4(1)	4(1)	6(2)

The observation of photoconductivity at visible wavelengths can be understood from the electronic structure obtained using ab initio modeling. We note that the calculated total one-electron density of states (DOS) well agrees with the valence band X-ray photoelectron spectrum, as seen in **Figure 4**a. This agreement gives us confidence in the analysis of the DOS projected on the atomic orbitals of each species, as shown in Figure 4b. The projected DOS suggests that there are several types of spin-up and spin-down optical transitions that are within the wavelength range used in our experiments. In all cases, the excited electrons are transferred to localized d-orbitals, while the holes either localize at Fe_B^{2+} ions, thus converting them into Fe_B^{3+} ions (for spin-down transitions), or delocalize at the top of the O 2p-derived portion of the band (for spin-up transitions). We note that differences in hole localization in the latter two cases are expected to manifest themselves in different time responses to photoexcitation, both at the excitation and recombination stages, which is consistent with our experimental data.

Based on the relative energies of the highest occupied spin-up O 2p and spin-down Fe_B^{2+} states, we propose that the fast current rise upon photoexcitation corresponds to excitations from the Fe_B^{2+} orbitals. Once these states are fully depleted, i.e., all Fe_B^{2+} is converted to Fe_B^{3+}, holes begin to occupy the O 2p band. Importantly, both the excited electrons and holes are available to contribute to the photocurrent. Conversely, once the light is turned off, the hole states at the top of the O 2p band are repopulated first. We propose that the persistent photoconductivity originates from the excited state configuration in which electrons reside at the Fe_A sites and holes at the Fe_B sites. Since the occupied spin-down Fe_B^{2+} t_{2g} and vacant spin-up Fe_A^{3+} t_{2g} states form the valence and conduction band edges, respectively, and are energetically close (<0.4 eV), electron hopping from Fe_B^{2+} t_{2g} band to Fe_A^{3+} t_{2g} is likely to occur, being driven by average thermal fluctuations. Since electron–hole recombination is suppressed by the spin-selection rules (see Figure 4b), the system adopts many nearly degenerate configurations, in which both of these bands are partially occupied and contribute to the electron transport.

Finally, we comment on the likelihood of Fe/Cr ordering in the B sublattice as depicted in the structural diagram in Figure 2a. Because Cr and Fe have very similar ionic radii (0.62 Å for Cr^{3+}, 0.65 and 0.78 Å for high-spin Fe^{3+} and Fe^{2+}, respectively),[26] a stochastic arrangement of Cr and Fe ions

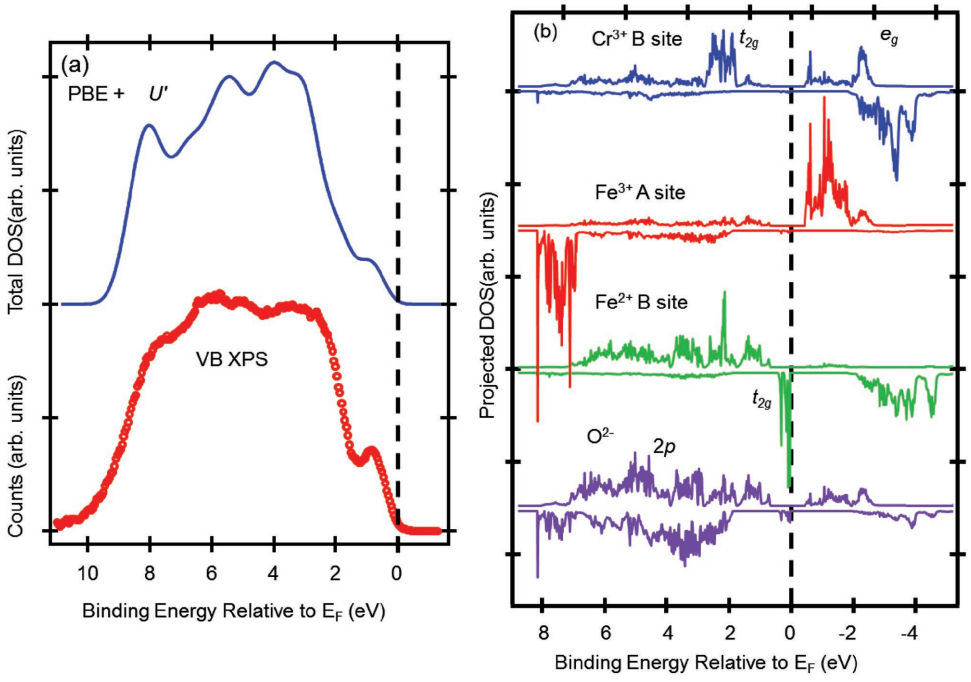

Figure 4. a) Calculated total density of states broadened by 0.05 eV (top) and experimental valence band X-ray photoelectron spectrum (bottom). b) One-electron density of states projected on the atomic orbitals for each ionic species at the relevant sites.

is reasonable to expect within the B-site sublattice. In this scenario, short-range segregation of Fe and Cr could also occur, and it is of interest to see if the Fe_A-to-Fe_B charge transfer mechanism would be operative in this case. **Figure 5** shows one such structure in which Cr^{3+} ions occupy two consecutive B-site planes and Fe^{2+} ions occupy the other two consecutive B-planes of a supercell. The total energy of this structure is only 0.2 eV per supercell higher than the energy of the supercell in which ordered Cr_B and Fe_B form the homogeneous, idealized structure shown in Figure 2a. Comparing the associated charge distribution with that in Fe_3O_4, we note that the Cr-rich region is positively charged, while the Fe_B-rich region is negatively charged. This implies that the $(Fe_A^{2+})_0(Fe_A^{3+})_1(Fe_B^{2+})_1(Fe_B^{3+})_0$ electronic configuration is metastable. Indeed, transfer of four electrons per cell from Fe_B to Fe_A sites, i.e., forming $(Fe_A^{2+})_{0.5}(Fe_A^{3+})_{0.5}(Fe_B^{2+})_{0.5}(Fe_B^{3+})_{0.5}$ configuration (b → c), results in a total energy gain of ≈0.5 eV per cell. Moreover, transfer of an additional four electrons per cell, i.e., forming the $(Fe_A^{2+})_1(Fe_A^{3+})_0(Fe_B^{2+})_0(Fe_B^{3+})_1$ configuration (c → d), corresponds to an energy cost of only 0.1 eV. These results suggest

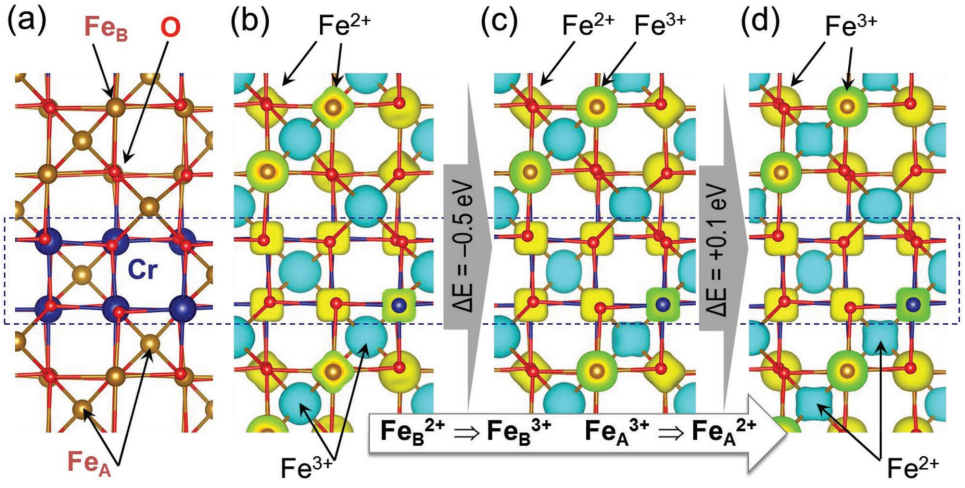

Figure 5. a) Atom positions and spin densities for three specific electron distributions over the Fe_A and Fe_B sites – b) $(Fe_A^{2+})_\gamma(Fe_A^{3+})_{1-\gamma}(Fe_B^{2+})_{1-\gamma}(Fe_B^{3+})_\gamma$: $\gamma = 0.0$, c) $\gamma = 0.5$, d) $\gamma = 1.0$. Fe, Cr, and O atoms are shown as brown, blue, and red spheres, respectively, in panel (a). Positive (spin-up) and negative (spin-down) isosurfaces of spin density are shown with yellow and cyan colors, respectively, in panels (b–d). The densities with color gradients are on the top surface of the super cell and are thus "sliced" in half as viewed in panels (b–d).

that various realizations of the $(Fe_A^{2+})_y(Fe_A^{3+})_{1-y}(Fe_B^{2+})_{1-y}(Fe_B^{3+})_y$ configurations can exist, thereby contributing to the electron conductivity via the mechanisms discussed above.

3. Conclusion

In summary, this investigation reveals that replacement of 1/3 of the Fe ions in Fe_3O_4 with Cr converts the material from a ferrimagnetic half metal to a ferrimagnetic semiconductor which is photoconductive in the visible portion of the electromagnetic spectrum. A conductive pathway quite different from that exhibited by Fe_3O_4 is shown to be energetically viable by ab initio modeling. The fact that Fe_2CrO_4 is photoconductive across the visible wavelength range makes this material attractive for photoelectrochemical applications.

4. First Principles Modeling

All calculations were performed using density functional theory with periodic boundary conditions. The Fe_2CrO_4 structure was represented using a 56-atom cubic cell containing eight A and 16 B cation sites. To examine the effects of substitutional disorder, we considered several nonequivalent configurations in which Cr atoms occupy A and B sites. For consistency, most of the calculations were performed for the structure in which Cr atoms occupy B sites of two consecutive (001) lattice planes. The calculations were performed using the Vienna Ab Initio Simulation Package.[27,28] The projected augmented wave method was used to approximate the core electron potential.[29] Exchange-correlation effects were treated using the Perdew–Burke–Ernzerhoff functional form[30] of the generalized gradient approximation (GGA) within the GGA+U scheme,[31] where the U correction applies to the Fe and Cr 3d states. The U values were optimized to reproduce characteristic features of the electronic structure (see Supporting Information); $U_{Fe} = 3.8$ eV and $U_{Cr} = 3.0$ eV. The plane-wave basis with a 500 eV cutoff was used. The calculations were performed using a $6 \times 6 \times 6$ Monkhorst–Pack k-point mesh with its origin at the Γ-point. The charge and spin density distributions were analyzed using the Bader method. The total energy was minimized with respect to the lattice parameters and internal coordinates. The energies of self-consistent calculations were converged to 10^{-6} eV per cell, and the lattice and atomic positions were relaxed until the forces on the ions were less than 0.02 eV $Å^{-1}$.

5. Experimental Section

All films (100 nm thick) were deposited by oxygen plasma assisted molecular beam epitaxy on MgO(001) at a temperature of 250 °C using a custom system from DCA Instruments (Finland). This approach is very similar to the one we used previously to successfully deposit $CoFe_2O_4$ films in which the Co^{2+} dopants exclusively occupy the B sites.[32] In situ XPS measurements were performed using a VG/Scienta R3000 analyzer and a monochromatic AlKα X-ray source. The Fe_3O_4 and Fe_2CrO_4 films were conductive and thus did not charge during XPS. As a result, the measured binding energies are correct in an absolute sense, having been calibrated against the Ag 3d and Fermi level from a polycrystalline Ag foil. Film composition analysis, along with structural parameters from ex situ X-ray diffraction, is given in the Supporting Information. EXAFS and XMCD were carried out at the Advanced Photon Source of Argonne National Laboratory using beamlines 20-BM-B and 4-ID-C, respectively. Electronic transport and magnetometry were carried out using a Quantum Design Physical Properties Measurement System. D.C. photoconductivity was measured using monochromatic light emitting dioides (Thorlabs, Inc.) between Pt wires 0.4 mm apart on the film surface.

Supporting Information

Supporting Information is available from the Wiley Online Library or from the author.

Acknowledgements

The PNNL work was supported by the U.S. Department of Energy, Office of Science, Division of Materials Sciences and Engineering under Award #10122 and was performed in the Environmental Molecular Sciences Laboratory, a national scientific user facility sponsored by the Department of Energy's Office of Biological and Environmental Research and located at PNNL. Calculations were performed using PNNL Institutional Computing (PIC) resources. This research also utilized the Advanced Photon Source, a U.S. Department of Energy (DOE) Office of Science User Facility operated for the DOE Office of Science by Argonne National Laboratory under Contract No. DE-AC02-06CH11357.

Received: September 27, 2016
Revised: November 19, 2016
Published online: January 13, 2017

[1] J. L. Dormann, M. Nogues, *J. Phys.: Condens. Matter* **1990**, *2*, 1223.
[2] S. E. Chamberlin, Y. Wang, K. Lopata, T. C. Kaspar, A. W. Cohn, D. R. Gamelin, N. Govind, P. V. Sushko, S. A. Chambers, *J. Phys.: Condens. Matter* **2013**, *25*, 392002.
[3] T. C. Kaspar, S. E. Chamberlin, M. E. Bowden, R. Colby, V. Shutthanandan, S. Manandhar, Y. Wang, P. V. Sushko, S. A. Chambers, *J. Phys.: Condens. Matter* **2014**, *26*, 135005.
[4] L. Qiao, H. Y. Xiao, S. M. Heald, M. E. Bowden, T. Varga, G. J. Exarhos, M. D. Biegalski, I. N. Ivanov, W. J. Weber, T. C. Droubay, S. A. Chambers, *J. Mater. Chem. C* **2013**, *1*, 4527.
[5] H. J. Yearian, J. M. Kortright, R. H. Langenheim, *J. Chem. Phys.* **1954**, *22*, 1196.
[6] H. J. Yearian, J. M. Kortright, R. H. Langenheim, *Phys. Rev.* **1954**, *95*, 653.
[7] W. D. Derbyshire, H. J. Yearian, *Phys. Rev. Lett.* **1958**, *1*, 427.
[8] W. D. Derbyshire, H. J. Yearian, *Phys. Rev.* **1958**, *112*, 1603.
[9] M. Mizumaki, A. Agui, Y. Saitoh, M. Nakazawa, T. Matsushita, A. Kotani, *Surf. Rev. Lett.* **2002**, *9*, 849.
[10] J. Ma, V. O. Garlea, A. Rondinone, A. A. Aczel, S. Calder, C. dela Cruz, R. Sinclair, W. Tian, S. X. Chi, A. Kiswandhi, J. S. Brooks, H. D. Zhou, M. Matsuda, *Phys. Rev. B* **2014**, *89*, 134106.
[11] M. Robbins, G. K. Wertheim, R. C. Sherwood, D. N. Buchanan, *J. Phys. Chem. Solids* **1971**, *32*, 717.
[12] J. Liu, Y. Liu, X. M. Chen, H. N. Dong, *Acta Physico-Chimica Sinica* **2009**, *25*, 107.
[13] A. Boudjemaa, R. Bouarab, S. Saadi, A. Bouguelia, M. Trari, *Appl. Energy* **2009**, *86*, 1080.
[14] S. A. Chambers, T. Droubay, *Phys. Rev. B* **2001**, *64*, 075410.

[15] T. C. Kaspar, S. E. Chamberlin, S. A. Chambers, *Surf. Sci.* **2013**, *618*, 159.
[16] G. S. Parkinson, *Surf. Sci. Rep.* **2016**, *71*, 272.
[17] R. Bliem, E. McDermott, P. Ferstl, M. Setvin, O. Gamba, J. Pavelec, M. A. Schneider, M. Schmid, U. Diebold, P. Blaha, L. Hammer, G. S. Parkinson, *Science* **2014**, *346*, 1215.
[18] S. Doniach, M. Sunjic, *J. Phys. C* **1970**, *3*, 285.
[19] E. Vescovo, H. J. Kim, J. M. Ablett, S. A. Chambers, *J. Appl. Phys.* **2005**, *98*.
[20] E. Goering, S. Gold, M. Lafkioti, G. Schutz, *Europhys. Lett.* **2006**, *73*, 97.
[21] E. J. Goering, M. Lafkioti, S. Gold, G. Schuetz, *J. Magn. Magn. Mater.* **2007**, *310*, E249.
[22] E. Stavitski, F. M. F. deGroot, *Micron* **2010**, *41*, 687.
[23] N. Menyuk, K. Dwight, R. J. Arnott, A. Wold, *J. Appl. Phys.* **1966**, *37*, 1387.
[24] P. K. Baltzer, P. J. Wojtowic, M. Robbins, E. Lopatin, *Phys. Rev.* **1966**, *151*, 367.
[25] B. M. Klahr, A. B. F. Martinson, T. W. Hamann, *Langmuir* **2011**, *27*, 461.
[26] R. D. Shannon, *Acta Crystallogr., Sect. A* **1976**, *32*, 751.
[27] G. Kresse, J. Furthmuller, *Phys. Rev. B* **1996**, *54*, 11169.
[28] G. Kresse, D. Joubert, *Phys. Rev. B* **1999**, *59*, 1758.
[29] P. E. Blochl, *Phys. Rev. B* **1994**, *50*, 17953.
[30] J. P. Perdew, A. Zunger, *Phys. Rev. B* **1981**, *23*, 5048.
[31] J. P. Perdew, K. Burke, M. Ernzerhof, *Phys. Rev. Lett.* **1996**, *77*, 3865.
[32] S. A. Chambers, R. F. C. Farrow, S. Maat, M. F. Toney, L. Folks, J. G. Catalano, T. P. Trainor, G. E. Brown, *J. Magn. Magn. Mater.* **2002**, *246*, 124.